PCCP

Accepted Manuscript

ROYAL SOCIETY OF CHEMISTRY

www.rsc.org/pccp

Journal Name

RSCPublishing

ARTICLE

Co-solvent Enhanced Zinc Oxysulfide Buffer Layers in Kesterite Copper Zinc Tin Selenide Solar Cells

Cite this: DOI: 10.1039/xoxxoooooox

K. Xerxes Steirer,[a*] Rebekah L. Garris,[a] Jian V. Li,[a] Michael J. Dzara,[b] Paul F. Ndione,[a] Kannan Ramanathan,[a] Ingrid Repins,[a] Glenn Teeter,[a] Craig L. Perkins[a]

Received ooth January 2012,
Accepted ooth January 2012

DOI: 10.1039/xoxxoooooox

www.rsc.org/

A co-solvent, dimethylsulfoxide (DMSO), is added to the aqueous chemical "bath" deposition (CBD) process used to grow ZnOS buffer layers for thin film $Cu_2ZnSnSe_4$ (CZTSe) solar cells. Device performance improves markedly as fill factors increase from 0.17 to 0.51 upon the co-solvent addition. X-ray photoelectron spectroscopy (XPS) analyses are presented for quasi-*in-situ* CZTSe/CBD-ZnOS interfaces prepared under an inert atmosphere and yield valence band offsets equal to -1.0 eV for both ZnOS preparations. When combined with optical band gap data, conduction band offsets exceed 1 eV for the water and the water/DMSO solutions. XPS measurements show increased downward band bending in the CZTSe absorber layer when the ZnOS buffer layer is deposited from water only. Admittance spectroscopy data shows that the ZnOS deposited from water increases the built-in potential (V_{bi}) yet these solar cells perform poorly compared to those made with DMSO added. The band energy offsets imply an alternate form of transport through this junction. Possible mechanisms are discussed, which circumvent the otherwise large conduction band spike between CZTSe and ZnOS, and improve functionality with the low-band gap absorber, CZTSe (E_g = 0.96 eV).

1. Introduction

Band energy lineups across thin film junctions and the ability to adjust resulting offsets are critical to the performance and optimization of photovoltaic devices. The band edge discontinuities that form between absorber/emitter materials are particularly important functional parameters for the absorber/buffer interface.[1] Yet, implementation of wide band gap buffer layers has proven difficult for junction formation with earth abundant absorbers. Kesterite $Cu_2ZnSn(S,Se)_4$ has been reported to have a large electron affinity and current blocking conduction band offsets (ΔE_C) with wide band bap buffer materials such as zinc sulfide and zinc oxysulfide (ZnO_xS_{1-x}) herein ZnOS.[2] Sakai et al. and Horoi et al. have reported on device performance for the pure sulfide, Cu_2ZnSnS_4 using a surface Sn enrichment procedure. This approach has led to improved PV devices. However, the CdS buffer layers outperform these alternate architectures.[3, 4] Another well known chalcogenide based PV technology has attained record high solar conversion efficiency, in part, through optimization of the Cu(In,Ga)Se_2/CBD-ZnOS heterojunction. [5] It is expected that the pure selenide $Cu_2ZnSnSe_4$, having a smaller E_g and higher electron affinity is incompatible with ZnOS due to the large positive discontinuity or "spike" in the conduction band lineup.

Among the well-studied buffer materials such as ZnS, In_2S_3, ZnO and CdS, the ZnOS alloy has several advantages including: i) large and controllable E_g; [6, 7] ii) processing routes including scalable vapor phase and chemical solution depositions; [8, 9] iii) elemental abundance with low cost and; iv) low toxicity of precursors and end-product. However, ZnOS also exhibits some properties considered as detrimental to implementation in solar cells including: i) low conductivity;[10] ii) insufficient control of electronically active defects and; iii) low extrinsic doping efficiency.[11] Yet, critical to window layer materials, ZnOS provides very high optical transmission. Hence, improved control of the electronic properties may allow for wider application to optoelectronics. If implemented through a CBD process, ZnOS could present a "drop in" replacement for smaller band gap CdS buffer layers.

High pH, aqueous CBD processes have led to high performance CIGS solar cells, in part because upon immersion into the CBD solution, alkaline cleaning of the absorber surface removes particles, surface oxides, and carbonaceous contamination, a process which has also been observed for CZTS.[1, 12] When compared to vacuum methods such as sputter deposition, CBD is considered "soft" meaning that incoming particles forming the interface are low energy and do not produce electronically active defects through ion impact. For some chalcogenides such as CIS and CIGS based PV devices, CBD-ZnOS has achieved superior performance in thin film solar cells.[5, 13] However, Barkhouse et al. reported a positive discontinuity or "spike" in the conduction band offset (CBO) between $Cu_2ZnSn(S_xSe_{1-x})_4$ and ZnOS close to 1 eV that renders an

impassible energy barrier for photogenerated electrons.[14] This heterojunction property is a major hurdle to implementation of wide band gap ZnOS buffer layers in CZTS solar technologies.

The very thin, nearly insulating ZnOS buffer layer (N ~ $1x10^{12}$ – $1x10^{14}$ cm^{-3}) is physically positioned between p-type CZTSe (N ~ $2.5x10^{16}$ cm^{-3}) and n-type i-ZnO (N ~ $1x10^{18}$ cm^{-3}).[15] Doping densities for the adjacent materials are larger and the absorber and window contact films are many times thicker in comparison, which renders the buffer layer strongly influenced by its neighbors. The layered structure depletes the buffer of charge and may populate or depopulate electronic defects in the buffer layer. For polycrystalline films, the optical, electronic and structural properties of the ZnOS alloy are well documented.[6, 16] Indeed, ordered ZnOS films exhibit E_g values that vary with the anion ratio from 3.2 for ZnO to 2.6 eV for $ZnO_{0.6}S_{0.4}$ and to 3.6 eV for ZnS. Several theoretical studies have examined the atomic and electronic band structure and band gap bowing versus the sulfur to oxygen ratio.[7, 17] Rozale et al. ascribe the band gap bowing effect to volume deformation, bond length deformation, and charge transfer due to the different electronegativities for oxygen and sulfur anions.[17] However, CBD-ZnOS thin films are often characterized as amorphous or poorly crystalline.

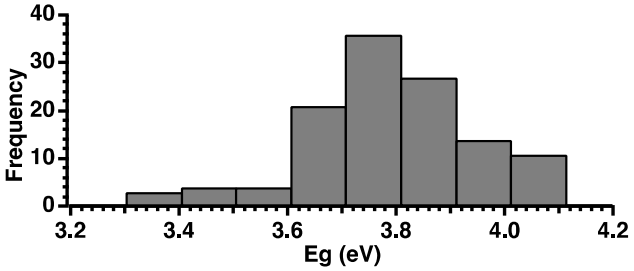

Fig. 1 Literature survey of optically measured E_g values obtained for ZnOS films plotted by solution concentrations for (a) zinc and (b) sulfur. (c) Histogram of CBD-ZnOS optical gap values.

Measured E_g values for CBD-ZnOS films are often large compared to binary ZnS and ZnO. The difficulty of depositing structurally ordered thin film ZnOS alloys by chemical solution deposition results from competing growth mechanisms guiding the film formation. Moreover, competition between differing nucleation and growth mechanisms in CBD can be quite sensitive to the details of the substrate surface roughness and chemical bonding mechanisms.[18] The use of additives for CBD thin films has been proposed to aid film growth and final film properties with potential advantages for manufacturing scale-up.[19] However, films grown on silicon based substrates of several varieties are not representative of those grown on absorber layers due to varying coverage and the apparent change to the growth mechanism from addition of the co-solvent dimethylsulfoxide (DMSO).[20]

A literature survey of optical band gap measurements for CBD-ZnOS is presented in Figure 1. Reported optical band gaps vary widely, and do not appear to correlate with the solution anion or cation molarity. The average is 3.79 ± 0.16 eV. Separating results that reported the inclusion of hydrazine results in similar E_g = 3.81 eV and 3.78 eV for depositions with and without hydrazine respectively. With literature reports of optical band gaps ranging from 4.1 eV to as low as only 3.3 eV, we conclude that well controlled CBD-ZnOS stoichiometry and corresponding optical properties have not been demonstrated to date. These are well above the minimum E_g of 2.6 eV for [S]/[S+O] ~ 0.4 using vapor deposition methods.[6-8, 16] Comparing these CBD reports with those for vapor deposited ZnOS, it seems likely that the most CBD-ZnOS films exhibit size quantization.[18] The CBD method is still lacking for applications where bulk ZnOS properties are desired. Complete notes, references and values are given in the supporting information file S1.

Devices with the configuration glass/Mo/CZTS(Se)/ZnOS/i-ZnO/Al:ZnO suffer severe performance loss due to the large, positive conduction band mismatch found at the CZTSe/ZnOS heterojunction. This "spike" in the conduction band lineup serves to block photocurrent as demonstrated by ultrafast UPS measurements reported by Barkhouse et al.[14] Yet unoptimized CBD-ZnOS deposited with the co-solvent DMSO enables high short circuit current (J_{sc}) and power conversion efficiencies over 5%. [21] In the present study, the effects of DMSO on ZnOS and the junction formed with CZTSe are compared using X-ray photoelectron spectroscopy derived band diagrams, admittance spectroscopy, and temperature dependent JV measurements (JVT). The surprising result that an increase of built-in potential leads to worse performing solar cells is discussed in reference to Fermi level pinning and alternate charge transport mechanisms in the buffer layer.

2. Results

2.1 CZTSe/CBD-ZnOS Characterization

Layer-by-layer growth of CBD-ZnOS on CZTSe was performed in a nitrogen-purged glove box interconnected with a UHV cluster tool. After each incremental deposition, the sample was rinsed in diluted NH_4OH in water followed by pure DI water (2.5% v/v) to eliminate $Zn(OH)_2$ precipitation onto the surface as described by Bär et al. [22] Rapid transfer to UHV (~ 2 min) without air exposure after growth steps ensured clean surfaces representative of each step during film growth.

2.1.1 X-ray Photoelectron Spectroscopy

XPS survey spectra for the CZTSe bare absorber and with ZnOS buffer layers of increasing thickness are presented in Figure 2. The thickness of the ZnOS buffer layer was increased by repeated immersion in fresh solution as detailed in the experimental section. Detected photoelectrons in spectrum (a) are emitted from elemental components of the bare absorber Cu, Zn, Sn and Se. Also observed is 1-2% adventitious oxygen on the CZTSe surface. The presence of oxygen on the CZTSe surface results after surface cleaning in dilute NH_4OH, which removes carbon surface contaminants and most oxides formed post-deposition.

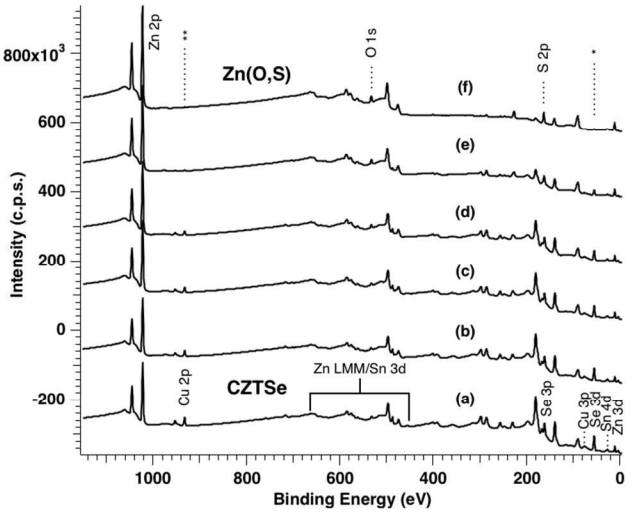

Fig. 2 XPS survey spectra for layer-by-layer formation of ZnOS/CZTSe heterojunction. (a) Clean CZTSe surface. CBD-ZnOS deposition times (b) 54 s, (c) 109 s, (d) 163 s, (e) 272 s and (f) 35 min onto the CZTSe shown in (a). See text for detailed explanation.

XPS performed on quaternary CZTSe exhibits multiple overlapping peaks with large spectral contributions from core levels and x-ray excited Se and Zn Auger photoelectrons. Ideally, XPS composition measurements utilize transitions with similar energy and probe depth. Therefore, Zn 3d, Cu 3p, Se 3d and Sn 4d core levels were used in the composition calculations, providing probe depths on the order of ~ 10 nm.[23] When compared to stoichiometric concentrations for Cu (25%), Zn (12.5%), Sn (12.5%) and Se (50%), Table 1 clearly shows a CZTSe surface that is rich in Zn and depleted of Cu and Sn. These films are terminated Zn rich during growth unlike the 1:1 Zn:Sn ratio reported by Sakai et al.[4] Zn over pressures during the final stages of deposition are used in high efficiency CZTSe solar cells to aid in carrier type inversion near the surface and to push the electronic depletion region further into the absorber and away from the metallurgical junction with the buffer and window contact.[24] The formal charges of +1 for Cu, +2 for Zn, +4 for Sn and -2 for Se, predict a net charge near zero for the measured surface composition of the Kesterite semiconductor. The observed Zn rich surface is likely to contain self-compensating $2Zn_{Cu} + Zn_{Sn}$ defect clusters as theoretically predicted by Chen et al.[25] If this defect structure is entirely responsible for the Zn rich surface, the predicted Cu/Sn ratio should be 2. However, the observed Cu/Sn ratio is 1.2, which indicates a likely excess of Zn_{Cu} point defects.

Another point of view is that the surface composition is nearly ZnSe with heavy Cu and Sn doping. As such, the surface composition is intermediate between CZTSe and ZnSe. In a related report, Erslev et al. showed that the composition of low-temperature deposited films can vary widely, with controllable optical and electronic properties.[26] Although the films studied here are deposited at 510ºC, it's possible that, to some extent a similar effect occurs under very Zn-rich conditions. While the exact nature of the CZTSe surface is still under debate, Zn enrichment preserves the Cu(I) and Sn(IV) dominant cation electronic character, minimizes Cu antisite defects and maintains predominant Kesterite semiconducting properties even as the stoichiometry evolves towards ZnSe. Further evidence for homogeneous CZTSe within the volume of the surface is given from Auger electron scanning microscopy down to the 100 nm length-scale (See Figure S2).

2.1.2 Buffer Layer Growth

Photoelectron intensity for the absorber elements Cu, Sn and Se attenuates as the thickness of the buffer layer increases with increasing CBD deposition time as shown in Figure 2. A key difference between the current study and XPS studies reported for ZnOS buffer layers on CIS, CGS and CIGS is the highly Zn rich composition of the underlying CZTSe that obscures the Zn-containing buffer. Signal attenuation of Cu 2p 3/2 (marked ** in Figure 2) occurs with shorter CBD times than for Se 3d 5/2 (marked * in Figure 2) at 932 eV and 54 eV binding energy (BE) respectively and is indicative of the difference in photoelectron escape depths at different kinetic energies. As the buffer thickness increases, the Zn Auger signal changes shape (discussed in detail later) and the O 1s and S 2p signal intensities increase. Upon 35 minutes of CBD, small but measureable substrate signal arising from the absorber is observed for the Se 3d, which is the lowest BE peak (highest kinetic energy (KE)) with high photoemission efficiency. This is observed for samples taken directly from device processing in ambient and for those deposited in-situ for surface analysis. Thickness measurements by other methods such as stylus profilometry and field emission scanning electron microscopy (FESEM) give thicknesses of 20 ± 4 nm. However, uniform ZnOS films of this thickness should completely attenuate photoelectron intensity from the underlying CZTSe and must be explained within the XPS results.

Sample	Cu (%)	Zn (%)	Sn (%)	Se (%)
CZTSe	6	38	5	50
		Zn	**O**	**S**
ZnOS water		50	13.5	36.5
ZnOS water+DMSO		50	14.0	36.0

Table 1 Elemental compositions of the CZTSe surface and the ZnOS buffer layers prepared with and without DMSO.

Attenuation analysis is used to address the nonuniform ZnOS coverage. Calculations using the TPP-2 formula for electron effective attenuation lengths (EAL) and the resulting thicknesses assuming a dense $ZnO_{1-x}S_x$ (x=0.73) alloy were performed using the National Institute of Standards and Technology (NIST) database. However, the experimental set-up for photoelectron detection in these studies used an acceptance angle of +/-7º and an inherently rougher surface than is typically done for flat single crystal substrates. Hence, the assumptions that predict signal attenuation for over-layers in this instance are only semi-quantitative and should be viewed as analytical means to assess coverage rather than an absolute measure of thickness. Spectra from high, medium and low BE regions were chosen for analysis. Considering the longest deposition time of 35 minutes and the fact that this results in signal barely observable from the absorber at low BE while higher BE signals are completely attenuated, then using the NIST PES EAL database, the calculated thickness of the buffer layer is 7.4 nm assuming a $ZnO_{0.27}S_{0.73}$ over-layer with density of 5.47 g/cm3 for an ordered crystal. However, the density of CBD films is typically lower than that of ordered crystals. D. Lincot and coworkers measured 4.1 g/cm^3 for the density of CBD-ZnOS deposited without hydrazine on a gold quartz crystal microbalance.[9] Using this value for the buffer layer density as input into the NIST PES EAL database gives a thickness value of 10 nm. Compared to EAL calculations, the measured thickness discrepancy is a factor of 2 resulting from factors such as substrate roughness and variations in buffer layer thickness. Voids and pinholes are not likely as shunting and V_{oc} loss

is not observed in device studies. However, nonuniform thickness of CBD-ZnOS buffer layers is observed in FESEM studies for CBD films on CZTSe. Therefore, we conclude that thin areas of the buffer layer allow a fraction of photoelectrons to pass through yet averages 20 nm thick.

Close inspection of the Zn LMM line shapes was performed in order to aid the composition analysis for ZnOS deposited on CZTSe (See S3). The Zn Auger parameter is a sensitive measure of the chemical state for Zn compounds and calculated for CZTSe and ZnOS at 2011.56 eV and 2010.76 eV respectively. The Auger parameter decreases by 0.8 eV due to the change in the chemical environment for Zn, commensurate with an abrupt shift in the surrounding composition. The Auger parameter for Zn in CZTSe has not yet been reported but the present measurement is very close to the reported value of 2011.5 eV for ZnSe.[27] As expected, the measured Auger parameter for ZnOS is between the literature values for ZnO and ZnS.[22] Note in Table 1 that the anion ratios for depositions with and without the co-solvent DMSO are nearly identical.

Further description of the ZnOS composition is made after close inspection of the O 1s spectral line shapes, shown in Figure 3. The oxygen detected on bare CZTSe was removed in the ammonia containing CBD whether CZTSe samples were as-received or pre-rinsed in dilute NH_4OH. For the 163 sec ZnOS deposition, the BE values from high to low are assigned to $Zn(OH)_2$ (532.75 eV), ZnOS alloy (531.67 eV). The initial layers of ZnOS on CZTSe appear rich in $Zn(OH)_2$. Measured BE values are in agreement with literature

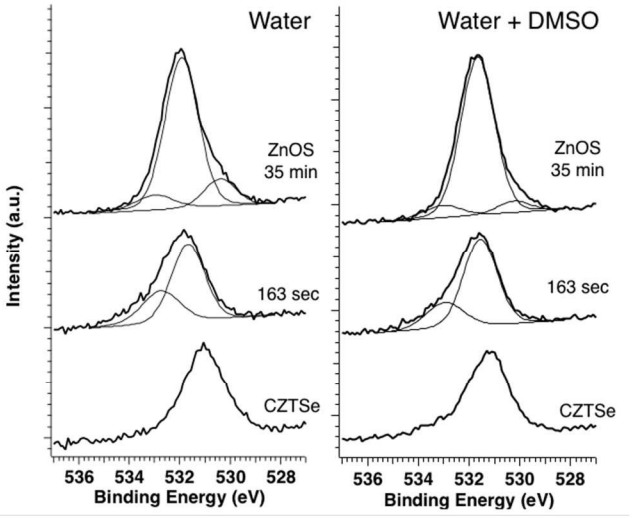

Fig. 3 O 1s spectral decompositions for CBD-ZnOS depositions with and without DMSO on CZTSe. Spectral contributions for O 1s surface contaminants were observed for surface oxygen on CZTSe cleaned with dilute NH_4OH.

values and indicate the dominant formation of alloyed ZnOS. Commensurate with the complex cluster growth mechanism, competition between zinc hydroxide and zinc ammonium complexes appears to initially favor the hydroxide. [22] While after nucleation the ammonium complexes dictate film growth, as growth of the film continues, incomplete sulfurization leaves the film composition with significant oxygen content. Model fits to spectra measured after 35 min depositions were allowed to shift according to the measured substrate core level shifts. Upon completion of ZnOS deposition, a new peak assigned to ZnO (530.4 eV) is observed in both cases. From the XPS results, the mole fraction x of oxygen in the film was 0.27. Inclusion of DMSO in the bath has little effect on the composition leading to x = 0.28. However, the O 1s line shape analysis indicates that the entirety of oxygen present is not alloyed and may contain a fraction of $Zn(OH)_2$ and ZnO. Additional spectra are available in Figure S4.

2.1.3 Band Energy Offsets and Band Bending

XPS core level and valence band spectra were measured for each surface in the layer-by-layer growth of ZnOS on CZTSe. The valence band maximum was measured at 0.6 eV below E_F and hence near midgap for the semiconductor. Upon growth of CBD-ZnOS onto CZTSe, the valence band maximum (VBM) signals superimpose until the substrate valence signal is attenuated and the VBM of ZnOS is revealed (See S5). The valence band offset (ΔE_V) is calculated using

$$\Delta E_V = (E_{CL}^{CZTSe} - E_{VBM}^{CZTSe}) - (E_{CL}^{ZnOS} - E_{VBM}^{ZnOS})_{thick} - (\Delta E_{CL}^{CZTSe} + \Delta E_{CL}^{ZnOS})_{thin} \quad (1)$$

Where, subscript CL represents a core level from either the CZTSe or ZnOS and subscripts thin and thick represent measurements taken from 163 sec and 35 min depositions of ZnOS on CZTSe. Core level shifts occur as E_F equilibrates across the junction during interface formation. This process is illustrated with spectra from the water only case in Figure 4 where the CZTSe core level BE values increase with ZnOS thickness, indicating a shift of the CZTSe VBM away from the Fermi energy. Note that ca. 0.4 eV of surface band bending is already present in the CZTSe due to the growth conditions. Representative Zn 2p 3/2, O 1s and S 2p 3/2 core level shifts for both water and water+DMSO cases are shown in Figure 5 versus deposition times for CBD with and without DMSO. For the water only case, most of the band bending induced core level shifts occur during the first few minutes of junction formation. The inclusion of DMSO lowers the average BE shift of the CZTSe core levels from 0.25 eV to 0.10 eV and thus lowers the effect of interface band bending in the absorber. Core level shifts for O 1s and S 2p closely

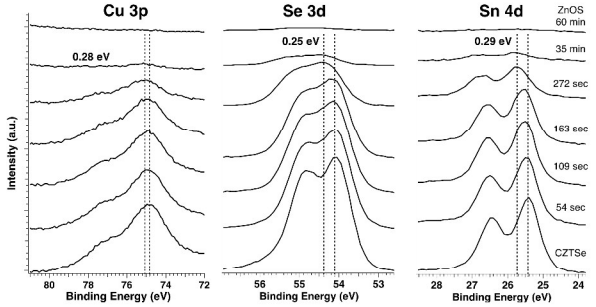

Fig. 4 Core level spectra from layer-by-layer growth of CBD-ZnOS on CZTSe using water solvent only.

followed those of the substrate as shown in Figure 5 indicating negligible (< 0.05 eV) band bending in the ZnOS buffer. Reproducible measurements for ΔE_V averaged for several different core levels of CZTSe (Cu 2p, Sn 4d, Se 3d) and ZnOS (O 1s, S 2p) result in the same ΔE_V equal to 1.0 ± 0.2 eV for growth conditions with and without DMSO. The larger positive change in the CZTSe core levels found in the case of the water only bath may be an indicator of larger n-type carrier density of the buffer layer. Ideally, the resultant band bending is equal to the difference in E_F before contact is made across the junction, however interface states or the presence of fixed charge may also contribute to the change in the observed band energy shifts.

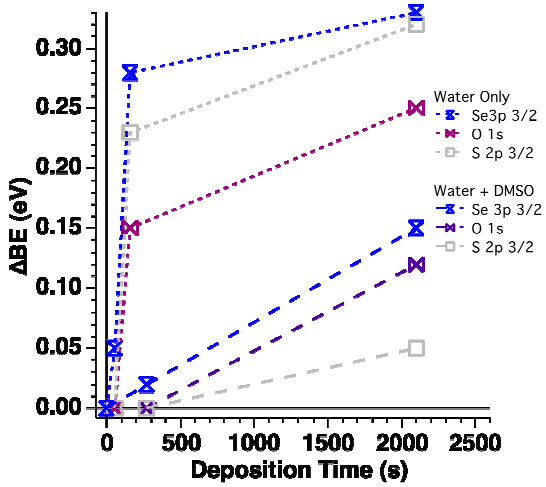

Fig. 5 XPS measured changes to the BE for Se 3p 3/2, O 1s and S 2p 3/2, which relate to the amount of band bending in CZTSe/CBD-ZnOS heterojunctions for water only and water+DMSO bath preparations. Lines are simply guides to the

A calculation of the CBO completes the band diagram, which would include the 0.96 eV optical gap of CZTSe. However, when photoemission spectroscopy (PES) and inverse PES are used to measure the surface electronic gap, it is increased to 1.2 eV following the growth procedure described by Repins et al.[24, 28] The optical E_g of CBD-ZnOS is 3.8 eV as described above and also in our previous reports.[29] Then calculation of the conduction band offsets (ΔE_C) follow

$$\Delta E_C = E_g^{ZnOS} - E_g^{CZTSe} + \Delta E_V \qquad (2)$$

The resulting ΔE_C for the CZTSe/CBD-ZnOS heterojunctions are 1.6 eV (± 0.4 eV) for CBD from water and water+DMSO. Clear differences in CZTSe band bending are present for the different bath conditions and the built in potential (V_{bi}) is expected to differ. However, this does not affect ΔE_V and ΔE_C in the present case. It is also important to note that the details of the buffer deposition vary significantly in literature. However, analyzing a large range of reported E_g for ZnOS (3.3 - 4.1 eV) the ΔE_C is expected in all cases to be equal to or larger than previously reported theoretical and experimental values for ZnS and ZnOS on CZT(S,Se) of 1.1 eV and 1.3 eV respectively.[14, 30]

2.2 Device Characterization

Completed photovoltaic devices with the layered structure glass/Mo/CZTSe/CBD-ZnOS/i-ZnO/Al:ZnO were characterized to assess the expected blocking properties of the buffer layers in solar cells operating under simulated one-sun conditions at 25ºC. The buffer effects on V_{bi} and JV versus temperature (JVT) were assessed to gain electronic information on the interface.

2.2.1 Solar Cell Performance

Transport measurements on CZTSe-based devices were used to explore the effects of the two different CBD processes on the ZnOS buffer layers. Overly thick buffer layers (30 nm) were used to minimize the possibility for shunts or pinholes to affect the shapes of the JVs shown in Figure 6. Except for the ZnOS, all depositions were performed in parallel to ensure identical material properties and robust trends. Note that the thick buffers lowered the performance metrics as compared to champion devices.

Devices with buffer layers (20 nm) that included DMSO in the ZnOS deposition reached over 5% power conversion efficiency (PCE) compared to CBD-ZnOS deposited from water only which gave PCE below 2%. Shown in Figure 6 are the JV responses for devices with the thicker buffer layers tested in dark and light conditions. Apparent in the light JV curve for the water only solvent is an inverted FF (< 25) as a result of the inflected JV. Detailed discussion of how buffer layers can cause JV-curve inflection and low FF in chalcogenide devices can be found in the literature.[31, 32] For the buffer layers deposited with DMSO added, solar cell measurements show no inflected JV curves when varying the thickness between 5 and 44 nm indicating that the inflection does not result from an overly thick buffer layer.[21] Including DMSO in the bath improves diode response and FF. Observed in the first quadrant of Figure 6 are crossed dark and light JV curves for the water only case, which indicates a barrier to electron transport. In contrast, inclusion of DMSO results in dark and light JVs that are aligned under forward bias.

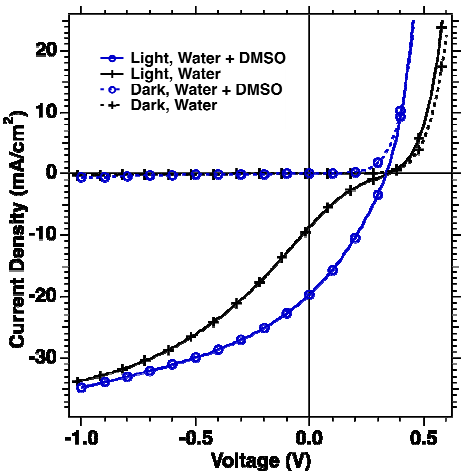

Fig. 6 JV curves for solar cells having thick buffer layers comparing bath preparations.

2.2.2 Admittance Spectroscopy and JVT

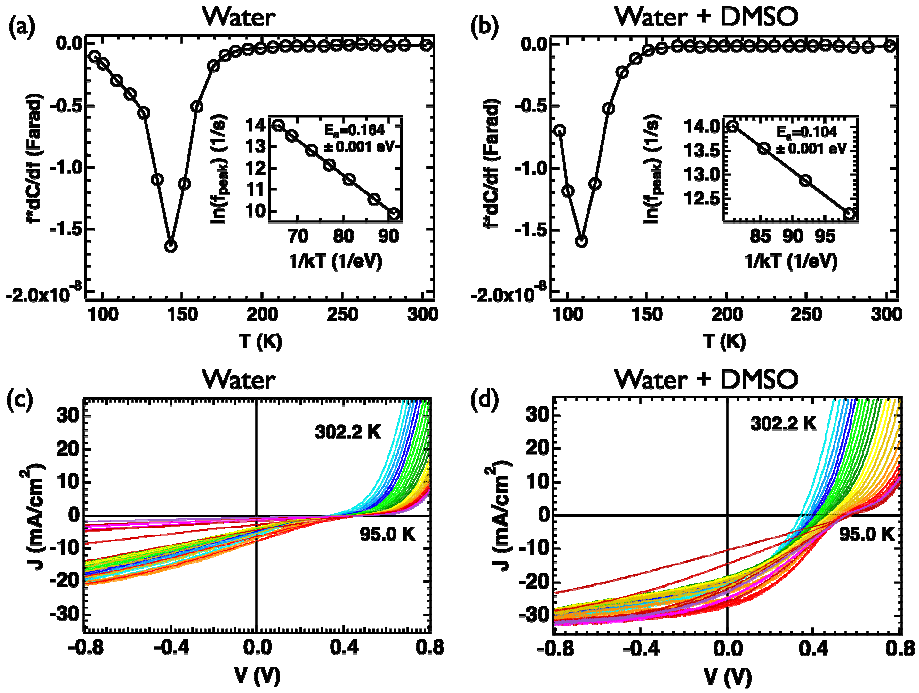

Fig. 7 Admittance showing temperature dependent carrier and mobility freeze out (a) and (b). JV vs. T showing increased CBO between ZnOS/ZnO in forward bias (c) and (d).

Admittance spectroscopy (AS) was performed on devices to assess the activation energies of dominant defects present. Data in Table 2 was acquired on the same samples used for JV measurements shown in Figure 6. Deposition of CBD-ZnOS with the different bath conditions results in identical room temperature V_{oc} values (0.336 V) and the nearly identical bulk E_F-E_V positions (0.167 to 0.170 eV) for CZTSe in the devices. As a reference, no dominant defect levels are observed when CdS is used as a buffer.[33] Hence, peaks located near 140 K and 105 K shown in Figures 7a and 7b respectively are electronic effects produced by inclusion of the CBD-ZnOS buffer layers. AS results differ slightly in the two samples, and the activation energy (E_a) is 60 meV larger for the CBD-ZnOS grown in the water only bath conditions. As a consequence of the sample and measurement, the E_a measured on these samples shown inset in Figure 7, is a signature of conductivity freeze-out, which is the combined effect of freeze-out of majority-carrier population and mobility. Note also that V_{bi} for the devices is increased for the seemingly more n-type buffer deposited from the water only bath. This increase is expected when considering the increased band bending shown in Figure 5. Differences in V_{bi} for these devices also correlate with the degree of band bending observed from XPS core level spectroscopy.

An assessment of the JVT measurements was performed under dark and illuminated conditions. Near 150ºC carriers in CZTSe begin to freeze out and strongly affect the JV response. Hence, our V_{oc}(T) analysis was performed on V_{oc}(T>150 K) providing analysis of the hole extraction barrier without the complication of temperature dependent collection efficiency. Hages et al. further modeled the effect of band edge potential fluctuations on V_{oc}, which can lower V_{oc} as the band positions become broadened.[34] However, a simple addition of DMSO to the buffer layer leaves the absorber band edge energy levels and associated potential fluctuations unchanged. Hence, measured V_{oc}(T=0 K) values reported in Table 2 represent changes in the ZnOS buffer layer that alter the interface dominated loss of photovoltage. Sheer described this Fermi level pinning effect at the absorber-buffer junction arising from either a continuum of energy state density or a discrete defect level.[35] Figures 7c and 7d show that the CBD-ZnOS made from the water only bath significantly lowers the low temperature photovoltage by 87 mV compared to that deposited from the water+DMSO bath conditions.

Sample	$E_{a,AS}$ (eV)	N_{cv} @0V, 300K, 10 kHz (1/cm3)	W_{cv} @0V, 300K, 10 kHz (um)	V_{bi} Band bend CZTS(V)	V_{oc} 300K (V)	V_{oc} T=0K 1 sun (V)	E_F-E_V bulk (eV)	ΔE_{CL} (eV)
Water	0.164	2.9e16	0.17	0.471	0.336	0.664	0.167	0.25
Water+DMSO	0.104	2.5e16	0.17	0.443	0.336	0.751	0.170	0.10

Table 2 Calculated electronic properties from V_{oc}(T), JVT and admittance spectroscopy.

3. Discussion

Band energy diagrams are presented in Figure 8, where the XPS derived band line-ups are shown with a slightly increased surface electronic gap of CZTSe as previously shown using inverse

photoelectron spectroscopy on these films.[28] Before contact is made to the buffer layer, thermally coevaporated CZTSe thin films grown using similar conditions exhibit a surface electronic gap of 1.2 eV as described above. Furthermore, the Fermi energy of the free surface is close to mid gap. After ZnOS deposition, with or without DMSO, the two CZTSe/ZnOS systems exhibit very large ΔE_C. Charge blocking ΔE_C for CIGS devices are known to result in inflected JV response and the crossing of dark and light JVs.[36] Reports from Minemoto et al., Sharbati et al. and others regarding inorganic thin film solar cells have shown the maximum allowable conduction band discontinuity is near 0.5 eV. Larger than this and J_{sc} drops precipitously.[37-39] A discontinuity for ΔE_C greater than 0.5 eV is sufficiently large to block photogenerated charge transport across the CZTSe/buffer heterointerface. The same is also known for CZTS based solar cells.[2] During JV measurement, as the negative bias is increased, the ΔE_C prevents photocurrent transport across the buffer layer (Quadrant IV). As the negative bias is further increased, the carrier density increases to the point that the ΔE_C is overcome and charge flows across the junction (Quadrant III). In Quadrant I, the crossing of dark and light JV curves arises when the illumination of the photovoltaic device modulates the ΔE_C, even if slightly, to change the charge injection efficiency between light and dark conditions under forward bias. For the water only case, both of these characteristics manifest in the performance tests. However, when DMSO is included in the bath, neither of these blocking ΔE_C effects are observed, indicating that the *apparent* ΔE_C is adequate for electron collection.

Considering the large ΔE_C for both CZTSe/CBD-ZnOS interfaces formed with and without DMSO and the apparent increase in n-type carrier density of the water only buffer deposition, one would expect nominally equal and poor device performance. One could argue that a slight improvement should be observed when the buffer layer induces higher band bending and V_{bi} is larger as in the water only case. However, the water+DMSO case exhibiting lower band bending and V_{bi} drastically improves device performance by removing the inflection of the JV response, increasing FF and eliminating dark/light crossing. From $V_{oc}(T)$ measurements, the extrapolated T = 0 K intercept is an indicator of the dominant recombination mechanism. In this case, the measured $V_{oc}(T = 0\ K)$ is far below E_g for the absorber. While both samples show interface dominated recombination, the effect in the water-only case is enhanced and results in a lower extrapolated V_{oc} at T = 0 K. From the above band line-up measurements, the compositional similarity, the differences in band bending and the device results, we hypothesize the existence of an alternate transport mechanism for

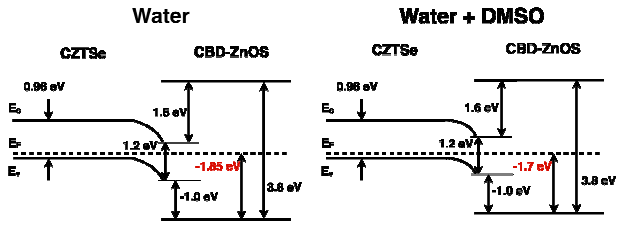

Fig. 8 Band Diagrams for CZTSe/CBD-ZnOS heterojunctions formed using water or water+DMSO as solvents in the buffer deposition.

which the severity or energy level can be changed by modifications to the CBD-ZnOS growth with the addition of DMSO.

High efficiencies for thin film CZTSe solar cells require optimal conduction band alignments with buffer materials. Sputter deposition of ZnOS demonstrated by Grimm et al. demonstrates that vapor growth methods allow for continuously variable anion alloying, x=[S]/[S+O] from 0 to 1 with commensurate control of E_g from 3.6 eV (x=1) to 2.6 eV (x=.45). This property control has positive effects on CIGS solar cells.[8] For CIGS absorbers, E_g is larger than that of CZTSe and control of ZnOS E_g through vapor deposition enabled high performance and systematic study of ΔE_C. The reported device data supports Minemoto et al. as well as Sharbati and Sites' device modeling treatments of thin film energy level alignments and the optimal alignment of ΔE_C.[37, 38] Yet for ZnOS, CBD does not provide facile control of E_g and other means are necessary to increase performance. Regarding the present case, the CZTSe/CBD-ZnOS compositional, spectroscopic and device studies point to charge transport that allows the buffer to act as a lower gap material with higher electron affinity as is shown schematically in Figure 9. The specific mechanism is unclear but may consist of: 1) Tunneling of electrons through thin areas of the buffer layer; 2) A defect band between 2.2 eV and 2.7 eV above the valence band maximum; 3) conducting ZnO filaments as shown by Hultqvist et al.[40]

In regards to electron tunneling, it is inefficient for length-scales beyond 3 nm, and would require much of the film to be thinner than the XPS attenuation analysis indicates. Moreover, the device studies used thicker CBD-ZnOS layers and identified that the effect is likely electronic and not purely morphological. Tunneling is therefore unlikely to contribute significantly to the present case.

Regarding defect mediated transport, no literature report has compared defect properties of ZnOS on thin film device performance, with most papers focusing on ZnOS growth, processing and efforts to tune E_g. However in a theoretical treatment, Varley et al. evaluated the electronic effects of point defects in ZnS and went so far as to study O, OH and H defects as well.[41] Hydrogen interstitials formed in ZnS were predicted as amphoteric defects 2.45

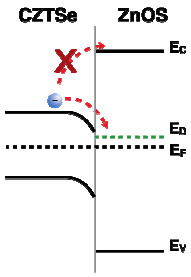

Fig. 9 Hypothesized alternate transport level (shown as discrete but may be continuous) that circumvents the large conduction band spike and allows the flow of negative photogenerated carriers across ZnOS/CZTSe heterojunction.

eV above the VBM, which may be stable at CBD processing temperatures. When lattice oxygen is substituted for sulfur and bound with interstitial hydrogen, the transition energy level is pushed even further towards the CBM leading again to an amphoteric defect. It remains to be demonstrated if these defects extrapolate to ZnOS films grown by CBD. Yet, identification and understanding the properties of these defects are critical to the implementation of ZnOS since they may act as performance limiting Shockley-Read-Hall recombination centers, fixed charge centers or clusters, which can alter the heterojunction electronic properties. Although speculative, the present example is one plausible atomistic

mechanism for the apparent sub-gap transport of charge in the CBD-ZnOS films.

The presence of ZnO filaments among the ZnOS buffer layer poses another interesting explanation. Regarding the energetics between ZnO and ZnS, Persson et al. reported theoretical ΔE_C of 1.06 eV for the isolated ZnS and ZnO materials and 0.6 eV for $ZnO_{0.25}S_{0.75}$ compared to ZnS.[42] Wei and Zunger calculated a larger ΔE_C of 1.54 eV.[43] This energetic offset could result in a significant DOS arising from ZnO that is far below the ZnOS CBM. Experimentally, the small ZnO related XPS O 1s spectral feature is observed for the ZnOS buffer layer deposited for 35 min. It is plausible that the right concentration of these conductive regions aids charge extraction and lowers the interface recombination.

Although other mechanisms may exist, either ZnOS point defects or ZnO secondary phases could form alternate charge conduction mechanisms. While DMSO is a dipolar, aprotic solvent and will not decompose in alkaline bath conditions, the present study demonstrates that manipulation of CBD-ZnOS electronic properties is possible by adding DMSO during film growth. The resulting changes to the buffer layer then facilitates high performance of an unlikely electronic junction partner such as ZnOS for applications limited by blocking ΔE_C such as in the case for thin film CZTSe solar cells.

4. Conclusions

When DMSO is substituted for a fraction of the water during chemical deposition, thin film ZnOS buffer layers grown on CZTSe exhibit marked electronic differences as measured with XPS, $V_{oc}(T)$ and JV(T). Anion ratios for these ZnOS films are similar and result in exceedingly large ΔE_C. However, the improved devices exhibit properties with an emitter having ΔE_C small enough to allow charge transport across the CZTSe/ZnOS interface and to the subsequent window contact layers. These measurements imply the presence of an alternate transport mechanism across the ZnOS buffer layer that is formed upon CBD with the co-solvent DMSO. Similar additives may expand the scope of CBD to consider materials for optoelectronic applications not previously suitable.

5. Experimental

5.1 ZnOS Deposition

Reagent grade zinc sulfate and thiourea (TU) were obtained from Sigma-Aldrich and used to prepare aqueous solutions of concentrations 0.075 M and 1.5 M, respectively. Reagent grade dimethyl sulfoxide (DMSO) and 28-30% ammonium hydroxide (NH_4OH) were all used as received. Deposition of ZnOS was carried out in a nitrogen purged glovebox. A jacketed beaker maintained the bath temperature at 80 ^oC. Reagents were added into the vessel in the order of DI, zinc sulfate, thiourea, and optionally, dimethylsulfoxide followed by initial heating for 10 minutes. 4.3 mL of NH_4OH was then added to the reaction solution and a sample was submerged. At the desired deposition time the sample was removed and immediately rinsed with a solution of 2.5% NH_4OH followed by DI water. Samples were dried with compressed nitrogen.

5.2 Photoelectron Spectroscopy

XPS measurements were performed under ultra-high vacuum (UHV) conditions (P_{base} better than 5×10^{-10} torr) within a Physical Instruments 5600 photoelectron spectrometer. X-ray excitation was generated with monochromatic Al K_α X-rays ($h\nu$ = 1486.6 eV). Pass energy for XPS was 11.75 eV. Compositions were calculated from background subtracted peak areas and corrected for each core level's relative sensitivity factor using Multipak software values. Fermi-energy calibration was performed using a freshly sputter cleaned Mo foil. Binding energy calibration followed Seah for Au 4f 7/2, Ag 3d 5/2 and Cu 2p 3/2 peak centriods. [44]

5.3 Profilometry

For thickness measurements, five small pieces of crystal bond were placed on the sample. The crystal bond was melted to formed small beads on the sample surface. Upon cooling to room temperature the samples were etched in a solution of 10% HCl for thirty seconds. The samples were then rinsed in DI and submerged in MEK for 20 minutes to dissolve the crystal bond, leaving isolated ZnOS spots to be measured using a Dektak profilometer.

5.4 Solar Cells

Solar cells were grown on soda-lime glass with sputtered Mo back contacts. CZTSe was thermally coevaporated using methods described previously with the inclusion of NaF deposited on the Mo back contact.[33] After CBD-ZnOS deposition onto the CZTSe, a sputtered bilayer i-ZnO/Al:ZnO top contact was followed by deposition of Ni/Al grids. Lithographic isolation defined device areas of 0.42 cm^2. Solar cell measurements were performed with simulated AM1.5 illumination while substrate temperature was held at 25ºC.

5.5 Admittance Spectroscopy and JVT

An Agilent 4294A impedance analyzer was used to conduct the capacitance-voltage (10 kHz, bias from -1.0 to +0.5 V) and admittance spectroscopy measurements (frequency from 1 to 1000 kHz; temperature from 70 to 310 K). The AC voltage modulation amplitude was kept at 55 mV peak to peak. We used an Agilent B2912A source-measurement unit for the current-voltage measurement with varying temperature (70 to 310 K) and light intensity (1×10^{-6} to 1 sun), the latter controlled by a set of neutral-density filters with a Newport 96000 solar simulator. The dark current-voltage measurements were taken at the same temperatures with the light from the solar simulator blocked by an aluminum plate.

Acknowledgements

This work was supported by the Laboratory Directed Research and Development (LDRD) Program at the National Renewable Energy Laboratory. MJD was supported by the U.S. Department of Energy, Office of Science, Office of Workforce Development for Teachers and Scientists (WDTS) under the Science Undergraduate Laboratory Internship (SULI) program. NREL is a national laboratory of the U.S. Department of Energy Office of Energy Efficiency and Renewable Energy (Contract No. DE-AC36-08-GO28308) operated by the Alliance for Sustainable Energy, LLC.

Notes and references

a National Renewable Energy Laboratory, Chemical and Materials Science, 1617 Cole Blvd., Golden, Colorado, 80401 USA. Email: Kenneth.Steirer@NREL.gov
b Rochester Institute of Technology, Chemical Engineering Dept., 1 Lomb Memorial Dr., Rochester, New York, 14623 USA.

1. J. Kessler, K. O. Velthaus, M. Ruckh, R. Laichinger, H. W. Schock, D. Lincot, R. ortega and J. Vedel, *PVSEC-6*, 1992, 1005-1010.
2. R. Haight, A. Barkhouse, O. Gunawan, B. Shin, M. Copel, M. Hopstaken and D. B. Mitzi, *Appl. Phys. Lett.*, 2011, **98**, 253502.
3. H. Hiroi, N. Sakai, S. Muraoka, T. Katou and H. Sugimoto, *38th IEEE PVSC Proceedings*, 2012, 001811-001814.
4. N. Sakai, H. Hiroi and H. Sugimoto, *36th IEEE PVSC Proceedings*, 2011, 003654.
5. Solar Frontier achieves record 20.9% cell efficiency on thin-film CIS, http://www.solar-frontier.com/eng/news/2014/C031367.html, (accessed August 5th, 2014).
6. B. K. Meyer, A. Polity, B. Farangis, Y. He, D. Hasselkamp, T. Krämer and C. Wang, *Appl Phys. Lett.*, 2004, **85**, 4929.
7. X. F. Fan, Z. X. Shen, Y. M. Lu and J.-L. Kuo, *New J. Phys.*, 2009, **11**, 093008.
8. A. Grimm, D. Kieven, R. Klenk, I. Lauermann, A. Neisser, T. Niesen and J. Palm, *Thin Solid Fims*, 2011, **520**, 1330-1333.
9. C. Hubert, N. Naghavi, A. Etcheberry, O. Roussel, D. Hariskos, M. Powalla, O. Kerrec and D. Lincot, *Phys. Status Solidi A*, 2008, **205**, 2335-2339.
10. J. M. Dona, *Journal of the Electrochemical Society*, 1994, **141**, 205.
11. M. Grün, A. Storzum, M. Hetterich, A. Kamilli, W. Send, T. Walter and C. Klingshirn, *Journal of Crystal Growth*, 1999, **201-202**, 457-460.
12. K. Ramanathan, J. Mann, S. Glynn, S. Christensen, J. Pankow, J. Li, J. Scharf, L. Mansfield, M. Contreras and R. Noufi, *38th IEEE PVSC Proceedings* 2012, 001677-001681.
13. T. Nakada and M. Mizutani, *Jpn. Journal of Appl. Phys.*, 2002, **41**, L165-L167.
14. D. A. R. Barkhouse, R. Haight, N. Sakai, H. Hiroi, H. Sugimoto and D. B. Mitzi, *Appl. Phys. Lett.*, 2012, **100**, 193904.
15. T. M. Hsieh, S. J. Lue, J. Ao, Y. Sun, W. S. Feng and L. B. Chang, *Journal of Power Sources*, 2014, **246**, 443-448.
16. S. K. Pandey, S. Pandey, A. C. Pandey and G. K. Mehrotra, *Appl. Phys. Lett.*, 2013, **102**, 233110.
17. H. Rozale, L. Beldi, B. Bouhafs and P. Ruterana, *Phys. Status Sol. B*, 2007, **244**, 1560-1566.
18. G. Hodes, *Phys. Chem. Chem. Phys.*, 2007, **9**, 2181.
19. N. Naghavi, D. Abou-Ras, N. Allsop, N. Barreau, S. Bücheler, A. Ennaoui, C. H. Fischer, C. Guillen, D. Hariskos, J. Herrero, R. Klenk, K. Kushiya, D. Lincot, R. Menner, T. Nakada, C. Platzer-Björkman, S. Spiering, A. N. Tiwari and T. Törndahl, *Prog. Photovolt: Res. Appl.*, 2010, **18**, 411-433.
20. M. Reinisch, C. L. Perkins and K. X. Steirer, - *in preparation*, 2015.
21. K. X. Steirer, R. L. Garris, C. Beall, A. Kanevce, K. Ramanathan, I. Repins, G. Teeter and C. L. Perkins, *40th IEEE PVSC Proceesings* 2014, 0847-0851.
22. M. Bär, A. Ennaoui, J. Klaer, T. Kropp, R. Sáez-Araoz, N. Allsop, I. Lauermann, H. W. Schock and M. C. Lux-Steiner, *Journal Appl. Phys.*, 2006, **99**, 123503.
23. C. J. Powell and A. Jablonski, *NIST Electron Effective-Attenuation-Length Database, v1.3, SRD 82*, National Institute of Standards and Technology, Gaithersburg, MD, 2011.
24. I. Repins, C. Beall, N. Vora, C. DeHart, D. Kuciauskas, P. Dippo, B. To, J. Mann, W.-C. Hsu, A. Goodrich and R. Noufi, *Solar Energy Materials and Solar Cells*, 2012, **101**, 154-159.
25. S. Chen, A. Walsh, X.-G. Gong and S.-H. Wei, *Adv. Mater.*, 2013, **25**, 1522-1539.
26. P. T. Erslev, M. R. Young, J. V. Li, S. C. Siah, R. Chakraborty, H. Du, R. J. Lad, T. Buonassisi and G. Teeter, *Sol. Energy Mat. Sol. Cells*, 2014, **129**, 124-131.
27. J. F. Moulder, W. F. Stickle, P. E. Sobol, K. Bomben and J. C. ed., *Handbook of X-ray Photoelectron Spectroscop 2nd ed.* , Perkin-Elmer Corporation, 1992.
28. I. Repins and M. Baer, personal communication.
29. J. Li, S. Glynn, S. Christensen, J. Mann, B. To, K. Ramanathan, R. Noufi, T. E. Furtak and D. Levi, *38th IEEE PVSC Proceedings*, 2012, 001580-001583.
30. A. Nagoya, R. Asahi and G. Kresse, *Journal of Physics: Condensed Matter*, 2011, **23**, 404203.
31. M. Buffière, G. Brammertz, S. Oueslati, H. E. Anzeery, J. Bekaert, K. B. Messaoud, C. Köble, S. Khelifi, M. Meuris and J. Poortmans, *Journal of Physics D: Applied Physics*, 2014, **47**, 175101.
32. A. O. Pudov, A. Kanevce, H. A. Al-Thani, J. R. Sites and F. S. Hasoon, *Journal of Applied Physics*, 2005, **97**, 064901.
33. J. V. Li, D. Kuciauskas, M. R. Young and I. L. Repins, *Appl. Phys. Lett.*, 2013, **102**, 163905.
34. C. J. Hages, N. J. Carter, R. Agrawal and T. Unold, *Journal of Applied Physics*, 2014, **115**, 234504.
35. R. Scheer, *Journal of Applied Physics*, 2009, **105**, 104505.
36. U. Rau and H. W. Schock, *Applied Physics A: Materials Science & Processing*, 1999, **69**, 131-147.
37. T. Minemoto, T. Matsui, H. Takakura, Y. Hamakawa, T. Negami, Y. Hashimoto, T. Uenoyama and M. Kitagawa, *Sol. Energy Mat. and Sol. Cells*, 2001, **67**, 83-88.
38. S. Sharbati and J. Sites, *IEEE Journal of Photovoltaics*, 2014, **4**, 697-702.
39. T. Unold and H. W. Schock, *Annu. Rev. Mater. Res.*, 2011, **41**, 297-321.
40. A. Hultqvist, C. Platzer-Björkman, E. Coronel and M. Edoff, *Sol. Energy Mat. and Sol. Cells*, 2011, **95**, 497-503.
41. J. B. Varley and V. Lordi, *Appl. Phys. Lett.*, 2013, **103**, 102103.
42. C. Persson, C. Platzer-Björkman, J. Malmström, T. Törndahl and M. Edoff, *Phys. Rev. Lett.*, 2006, **97**, 146403.
43. A. Zunger, *Appl. Phys. Lett.*, 2003, **83**, 57.
44. M. P. Seah, *Surf Interface Anal*, 1989, **14**, 488-488.